Coatings **2014**, *4*, 527-552; doi:10.3390/coatings4030527

OPEN ACCESS

coatings

ISSN 2079-6412

www.mdpi.com/journal/coatings

Article

Wetting, Solubility and Chemical Characteristics of Plasma-Polymerized 1-Isopropyl-4-Methyl-1,4-Cyclohexadiene Thin Films

Jakaria Ahmad [1], Kateryna Bazaka [1], Michael Oelgemöller [2] and Mohan V. Jacob [1,*]

[1] Electronic Materials Research Lab, College of Science, Technology and Engineering, James Cook University, Townsville 4811, Australia; E-Mails: jakaria.ahmad@my.jcu.edu.au (J.A.); katia.bazaka@jcu.edu.au (K.B.)

[2] Applied and Green Photochemistry Group, College of Science, Technology and Engineering, James Cook University, Townsville 4811, Australia; E-Mail: michael.oelgemoeller@jcu.edu.au

* Author to whom correspondence should be addressed; E-Mail: mohan.jacob@jcu.edu.au; Tel.: +61-7-4781-4379.

Received: 8 April 2014; in revised form: 11 July 2014 / Accepted: 22 July 2014 / Published: 31 July 2014

Abstract: Investigations on the wetting, solubility and chemical composition of plasma polymer thin films provide an insight into the feasibility of implementing these polymeric materials in organic electronics, particularly where wet solution processing is involved. In this study, thin films were prepared from 1-isopropyl-4-methyl-1,4-cyclohexadiene (γ-Terpinene) using radio frequency (RF) plasma polymerization. FTIR showed the polymers to be structurally dissimilar to the original monomer and highly cross-linked, where the loss of original functional groups and the degree of cross-linking increased with deposition power. The polymer surfaces were hydrocarbon-rich, with oxygen present in the form of O–H and C=O functional groups. The oxygen content decreased with deposition power, with films becoming more hydrophobic and, thus, less wettable. The advancing and receding contact angles were investigated, and the water advancing contact angle was found to increase from 63.14° to 73.53° for thin films prepared with an RF power of 10 W to 75 W. The wetting envelopes for the surfaces were constructed to enable the prediction of the surfaces' wettability for other solvents. The effect of roughness on the wetting behaviour of the films was insignificant. The polymers were determined to resist solubilization in solvents commonly used in the deposition of organic semiconducting layers, including chloroform and chlorobenzene, with higher stability observed in films fabricated at higher RF power.

Keywords: coatings; wetting; plasma polymerization; FTIR; contact angle

1. Introduction

Organic thin film materials have many potential and implemented applications, from biocompatible and antifouling coatings in medical devices to protective coatings, waveguides and component materials in optoelectronic devices, such as flexible organic electroluminescent devices (OLED), organic photovoltaics (OPV) and organic thin film transistors (OTFT) [1–6]. The motivation for using organic materials stems from their chemical versatility, low cost, low temperature fabrication and ability for reel-to-reel printing, as well as mechanical flexibility [1]. The attractive synthetic and processing flexibility of organic materials allows for fine tuning of their properties to achieve a desired combination of optoelectronic, physicochemical, mechanical and biological characteristics, and controlling the manner in which these materials interact with relevant liquids [7]. The latter is an important aspect for optoelectronics and biomedical applications alike. Solution processing of electronic circuits demands dielectric interlayer stability in organic solvents and strong interfacial adhesion, while the susceptibility of the coating to the uptake of moisture is critical for OPV encapsulation applications. Surface wetting by physiological fluids is a key determinant of biocompatibility and degradation under *in vitro* and *in vivo* conditions [1,8]. The surface-solvent kinetics and ensuing degradation of organic materials under aqueous conditions is an important consideration for biodegradable and compostable electronics, where it would affect both operational performance and the physical transience of the device [9].

One of the key predictors of surface-solvent interactions, the wetting behaviour at polymer surfaces and interfaces, is dependent on the nature of the variable length of polymer chains, density fluctuations and the relatively slow motion of the long chain molecules [10]. Contact angle (CA) analysis is typically used to obtain primary data from which the degree of wettability for a specific solid-liquid combination can be inferred [7,11], with lower CAs indicating better wetting compared to larger CAs. This analysis also provides indirect information about the structure of the film matrix, where observed changes to θ at the liquid/solid interface are attributed to specific solid-liquid interaction mechanisms, such as absorption, spreading and swelling [12]. Fundamentally, wettability is affected by the chemical composition, topography, rigidity and homogeneity of the surfaces. The chemical composition of the surface determines its surface energy: whereas surfaces rich in non-polar groups (e.g., $–CH_x$, with $x = 1–3$) have low surface energies and, thus, are hydrophobic, surfaces with a high density of polar groups (e.g., –OH or –C=O) exhibit high surface energies and are hydrophilic [13]. With regard to surface topography, an increase in the surface roughness enhances the surface hydrophilicity of hydrophilic materials and hydrophobicity in the case of hydrophobic surfaces [14]. The micro- and nano-scale variations in the slope on the surface are believed to create physical barriers that directly affect the motion of the contact line, thus affecting CAs observed at the macro scale. In a similar way, distinct domains of chemically heterogeneous surfaces, e.g., those with higher hydrophobicity, are thought to interfere with the motion of the contact angle by hindering the advancement or contraction of the water front and, thus, increasing or decreasing the observed CA. Several models propose a relationship between the measured CAs of a given non-ideal surface and its flat, homogenous

counterpart of the same composition, among them Wenzel and Cassie–Baxter models [15,16]. In the Wenzel model, the liquid is assumed to be in contact with all of the parts of the irregular surface and is typically applied to chemically homogenous surfaces, whereas the Cassie-Baxter model places the drop on the surface protrusions without wetting the entire surface and is believed to be more appropriate for chemically heterogeneous surfaces.

Recently, growing interest in environmentally-friendly technologies has led to the exploration of a number of alternative organic source materials, e.g., unprocessed raw agricultural, food and waste substances [17], and energy-efficient green fabrication methodologies, e.g., plasma-assisted nanofabrication [18,19]. The key driver of this research therefore rests in the need to support robust and sustainable economic and societal development, which, in practical terms, means the development of materials and technologies that are cheaper, more efficient and can address the objectives of modern societies in an environmentally-sustainable fashion. Most of the existing chemical synthesis processes used for the fabrication of electronics device components are energy-inefficient and require multi-step processing and the use of hazardous auxiliary substances, such as organic solvents and catalysts [20]. These synthesis routes often rely on expensive and/or toxic, high purity, non-renewable materials [1]. In addition to using hazardous materials, modern electronic devices also use valuable and scarce materials, the availability of some of which (e.g., gallium, indium, *etc.*) is reducing at a high rate [1]. At the same time, only a limited portion of high-tech waste is recycled, with the bulk of the waste being deposited into landfills, where it slowly degrades, leaching out potentially harmful by-products. By using minimally processed, renewable natural resources, such as non-petrochemical oils, e.g., essential oils, and highly reactive non-equilibrium dry plasma-based chemistry, it is possible to lower the environmental footprint and the economic costs of organic electronics and other such technologies throughout their lifecycle, from their fabrication to their use and disposal [21].

Essential oils are volatile aromatic compounds that are widely used in pharmacological, perfumery and culinary preparations for their aromatic and medicinal properties. Their availability in commercial quantities, relative low-cost, renewable nature and minimal toxicity makes them a suitable precursor for "green" functional materials [22]. As a volatile material, essential oil is well suited to chemical vapour deposition (CVD), as no carrier gas is required to deliver the monomer into the polymerization chamber. Using plasma as a catalyst, the oils can be converted into functional polymer thin films in a one-step process at room temperature, without the need for pre- or post-processing, e.g., annealing, or catalysts. Unlike most plasma deposited films, plasma polymers of essential oils are optically transparent and smooth. Over the last few years, thin films from lavender and tea tree essential oils have been developed and identified as promising candidates for applications in electronics, as dielectric and encapsulation layers [23–27]. Plasma polymers of terpinen-4-ol also display a valuable and rare electron blocking hole-transporting property that is very attractive for OLEDs [27]. Versatile biological activity, including antibacterial activity against drug-resistant strains of *Staphylococcus*, *Streptococcus* and *Candida* species, also makes essential oils an attractive candidate for the fabrication of antibacterial and biocompatible implantable systems, including implantable electronics [28].

This paper reports the fabrication of polymer thin films from 1-isopropyl-4-methyl-1,4-cyclohexadiene, also known as γ-Terpinene, using RF plasma polymerization. γ-Terpinene is an isomeric hydrocarbon distilled directly from *Melaleuca alternifolia* essential oil and used extensively in cosmetics and cleaning products for its aromatic and medicinal properties. While γ-Terpinene has been determined as a

component in plants using many quantitative analysis methods [29,30], it had not been studied extensively as the main topic compound [31]. However, recent investigations of γ-Terpinene revealed that the optical properties of the fabricated plasma-polymerized γ-Terpinene (pp–GT) thin films are promising, with transparency to the optical wavelengths and refractive index of 1.57–1.58 (at 500 nm) [26]. It is reported that these polymers possess an optical band gap (E_g) of ~3 eV that falls into the insulating E_g region. Independent of deposition conditions, the surfaces are smooth and defect-free, with uniformly distributed morphological features and average roughness well below 0.30 nm [26]. The optical and surface characteristics suggest that the pp–GT thin films have the potential to be implemented in optoelectronic and insulating applications. This paper focuses on the wetting, solubility and chemical characteristics of these films and the compatibility of the material with solvents typically utilized in the manufacturing of organic electronic devices, with the intention to use these films in OPVs, especially as encapsulation coatings and insulating layers in flexible electronics.

2. Experimental Section

2.1. Preparation of Thin Films

Thin film samples were deposited on high quality glass microscope slides using a custom-made RF polymerization chamber, 0.75 m in length with an inner diameter of 0.055 m (volume of 0.0035 m^3). RF power is delivered to the system via an ENI RF generator at 13.56 MHz through a matching network and capacitively coupled copper electrodes. The copper electrodes were placed 0.11 m from the monomer inlet and 0.1 m apart, with the active electrode closest to the monomer inlet. The electrode configuration used was based on the uniformity of the RF discharge it produced and the corresponding uniformity of resulting thin films for the particular reaction chamber utilized throughout this work.

Prior to deposition, the substrates were thoroughly washed in extran, cleaned ultrasonically in water, rinsed in isopropanol and distilled water, air dried and placed in the reaction chamber. For each deposition, 5 mL of γ-Terpinene (GT) monomer was used. The chamber was evacuated to a pressure of ~100 mTorr, at which stage the monomer inlet was opened to allow the monomer to evaporate. Argon gas was then used to flush the chamber for 1 min at a pressure of 1000 mTorr to remove residual background gas and ensure an oxygen-free surface. The chamber was then evacuated to 100 mTorr, at which stage the monomer inlet was closed, and RF glow (10, 25, 50 and 75 W) was initiated. The monomer-free plasma state was maintained for 2 min to stabilize the pressure, as well as to etch potential residual contaminants from the surface of the substrate. Once the pressure had reached 150 mTorr, the monomer inlet was opened, beginning the deposition. The flow rate was controlled via a vacuum stopcock and was estimated to be 1.57 cm^3/min by employing the procedure outlined by Gengenbach and Griesser [32].

Following the aforementioned experimental procedure, plasma polymer thin films were fabricated from γ-Terpinene (GT) monomer (Figure 1) at various RF power levels (10, 25, 50 and 75 W) and an ambient temperature of 20 °C. pp–GT thin-films were examined over the wavelength range 190–1000 nm using a variable angle spectroscopic ellipsometer (model M-2000, J.A. Woollam Co., Inc., Lincoln, NE, USA). Ellipsometric parameters Ψ and Δ were obtained at three different angles of incidence, φ = 55°, 60° and 65°. In addition, the transmission data were also collected. Ψ and Δ were

used to derive the optical constants based on a multilayer model consisting of a previously modelled substrate and Cauchy layer built in the J.A. Woollam Inc. analysis software (WVASE32) [33] via regression analysis. The quality of the fit was measured quantitatively by determining the mean-squared error and through the use of the correlation matrix. Gaussian oscillators were employed within the model to provide an optimal fit of the data, with a lower mean square error and lower average correlation between fitting terms. A more detailed review of the procedure has been reported elsewhere [34]. Samples for Fourier transform infrared (FTIR) and CA measurements were deposited for 30 min to obtain films of ~700 nm thickness. Depositions were performed for 45 min to obtain films of ~1 μm for atomic force microscope (AFM) measurements.

Figure 1. Conformers of 1-isopropyl-4-methyl-1,4-cyclohexadiene resulting from the rotation about the C^7–C^1 bond, adapted from [35].

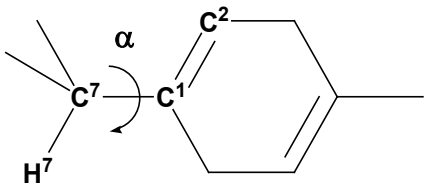

2.2. Chemical Characterization

FTIR spectroscopy was carried out for the chemical characterization of the γ-Terpinene monomer and the pp–GT thin films using a Perkin Elmer Spectrum 100 FTIR spectrometer. Spectra were obtained in transmission mode in the region of 4000–500 cm^{-1}, where 32 scans were acquired for each sample at a resolution of 1 cm^{-1}. Contributions from CO_2 and H_2O were eliminated from the spectra by a background subtraction procedure, where the background was pre-recorded under the same atmospheric conditions.

The surface chemistry of the deposited samples was further analysed by XPS on a SPECS SAGE XPS system equipped with a Phoibos 150 hemispherical analyser and an MCD-9 detector. The background pressure was held at 2×10^{-6} Pa during experiments. For wide scan spectra and high resolution scans of the C 1s peak, an Mg Ka X-ray source was used ($h\nu$ = 1253.6 eV), operated at 10 kV and 20 mA (200 W). Measurements were performed with a pass energy of 100 eV, and 0.5 eV energy steps were used for wide scan spectra, while 20 eV pass energy and 0.1 eV energy steps were used for high resolution scans. Spectra were analysed using CasaXPS (Case Software Ltd, Teignmouth, UK). Synthetic peaks were fitted to the C 1s envelops following the methodology of Beamson and Briggs [36] with the spectra correction for charging effects during analysis using a reference value of 285 eV, the binding energy of the C–C component from neutral hydrocarbon [37]. The analysis area was circular with a diameter of 5mm, and spectra were acquired at a take-off angle of 90°.The full width at half maximum (FWHM) of the C 1s synthetic peaks remained constant at 1.5 eV.

2.3. Contact Angle (CA) Measurements

Static and dynamic CAs (using water, diiodomethane (DIM) and ethylene glycol (EG) as probing liquids) of pp–GT thin films are measured. Static CAs are commonly used in calculations of surface

tension parameters. However, they may not provide a reliable description of a non-ideal surface, *i.e.*, that is chemically and/or morphologically heterogeneous. Plasma-modified and plasma-polymerized surfaces are often characterized by both chemical and morphological heterogeneity [38]. Non-ideal surfaces typically display hysteresis, which can be estimated by measuring advancing and receding CAs.

CA measurements were performed using a KSV 101 system and a micrometre syringe with a narrow diameter stainless steel needle. The static CA was measured by the sessile drop method, whereby a drop of probing liquid was gently placed onto the thin film surface. The apex of each drop was confirmed using a CCD camera prior to each measurement to ensure consistency in drop volume (8 μL). The evolution of the CA (θ, the angle between the baseline of the drop and the tangent at the drop boundary), the droplet volume (V, μL), the droplet surface area (A, mm^2), the droplet height (h, mm) and the droplet basal diameter ($2r$, mm) were monitored using a software-assisted image-processing procedure. The reported values are an average of a minimum of seven measurements taken for each examined surface.

Advancing and receding contact angles were measured using the dynamic sessile drop technique. First, a sessile drop of probe liquid of known volume was placed on the surface of the sample, ensuring that the needle remained in the drop during the measurement to avoid undesired vibration. The drop was then modified by slowly adding volume, with the advancing angle estimated as the largest contact angle possible without increasing its solid/liquid interfacial area. The receding angle was estimated as the minimum possible angle that can be achieved by slowly removing the probe liquid from the drop without decreasing the drop's contact area. Both the advancing and receding angle were estimated as the average of the angles on both sides of the drop profile. Contact angle hysteresis (CAH) was estimated as the difference between the advancing and receding angle.

The presence of the needle is known to distort the contour line of the drop, due to the interactions between the surface of the needle and the liquid with the drop. The distortion of the drop shape is more prominent in the case of receding angles, where the needle's receding angle tends to pull the drop up around the needle. This distortion may result in significant errors [39].

2.4. Surface Free Energy Analysis

There are several widely applied approaches for the determination of the solid surface free energy and its components from CA measurements [40]. Most theories of solid surface energy have a basis in Young's equation that employs the equilibrium CA, where the solid is considered close to ideal. The ideal surface is one that is chemically and morphologically homogenous, and thus, CAH is assumed to be absent or negligible.

For the non-ideal surfaces that are chemically and morphologically inhomogeneous, with a measurable, substantial CAH, the apparent surface free energy γ_{SV} and other interfacial interaction parameters, adhesive film tension Π, work of adhesion W_A and work of spreading W_S, can be derived from the CAH approach developed by Chibowski [41] with only three measurable quantities: the surface tension of the probe liquid γ_{LV} and its advancing θ_A and receding θ_R CA hysteresis ($CAH = \theta_A - \theta_R$). The solid surface free energy γ_{SF} can be expressed by the following relation [41]:

$$\gamma_{SF} = \gamma_{SV} + \Pi \quad (1)$$

$$\Pi = \gamma_{LV}(\cos\theta_R - \cos\theta_A) \quad (2)$$

The apparent, total surface free energy of a solid γ_{SV} ($\approx \gamma_{SF}$) can be expressed as [41]:

$$\gamma_{SV} = \frac{\Pi(1+\cos\theta_A)^2}{(1+\cos\theta_R)^2 - (1+\cos\theta_A)^2} \quad (3)$$

CAH can be related to the work of spreading W_S of liquid on the polymer surface. W_S is a thermodynamic quantity that relates the wettability to the mechanical strength of adhesion. It enables one to characterize the competition between solid-liquid adhesions with different liquids [40]. W_S can be easily calculated from the work of adhesion W_A and the work of cohesion W_C:

$$W_S = W_A - W_C \quad (4)$$

where $W_A = \gamma_{LV}(1 + \cos\theta_A)$ and $W_C = 2\gamma_{LV}$ [40].

For surfaces that are chemically heterogeneous, but very smooth, the experimentally observed advancing CA θ_A might be expected to be a good approximation of Young's CA θ_Y, whereas the experimental receding angle, θ_R, is expected to have less reproducibility, due to liquid sorption or solid swelling [39]. With the assumption of $\theta_A = \theta_Y = \theta$, the surface free energy can be calculated by means of the van Oss' adaptation of Young's theory [42,43]. The quantitative determination of all of the surface thermodynamic properties of the polymer coatings was performed using the Young-Dupré equation [43]:

$$(1+\cos\theta_a)\gamma_L = 2\left(\sqrt{\gamma_s^{LW}\gamma_L^{LW}} + \sqrt{\gamma_s^+\gamma_L^-} + \sqrt{\gamma_s^-\gamma_L^+}\right) \quad (5)$$

where θ_a is the advancing CA (°), γ_L is the surface tension (SFT) of the liquid in contact with the solid surface (mJ/m^2), γ_L^{LW} is the apolar component (Lifshitz–van der Waals [LW]) of the SFT of the liquid (mJ/m^2), γ_L^+ is the electron-acceptor parameter of the polar component (acid–base [AB]) of the liquid (mJ/m^2), γ_L^- is the electron-donor parameter of the polar component (AB) of the liquid (mJ/m^2), γ_s^{LW} is the apolar component (LW) of the surface energy of the solid (mJ/m^2), γ_s^+ is the electron-acceptor parameter of the polar component (AB) of the solid (mJ/m^2) and γ_s^- is the electron-donor parameter of the polar component (AB) of the solid (mJ/m^2).

The interface interaction of the polymer and the solvent is determined from their interfacial tension γ_{12} using the following equation [43]:

$$\Delta G_{121} = -2\gamma_{12} \quad (6)$$

where ΔG_{121} is the free energy change. In the case of two completely miscible substances, where the interfacial tension cannot be measured directly, γ_{12} can be calculated using the following equation:

$$\gamma_{12} = \left(\sqrt{\gamma_1^{LW}} - \sqrt{\gamma_2^{LW}}\right)^2 + 2\left(\sqrt{\gamma_1^+\gamma_1^-} + \sqrt{\gamma_2^+\gamma_2^-} - \sqrt{\gamma_1^+\gamma_2^-} - \sqrt{\gamma_1^-\gamma_2^+}\right) \quad (7)$$

In case of two completely immiscible substances (or any given solid-liquid system), the interfacial tension can be derived directly from the measured contact angle θ:

$$\gamma_{SL} = \gamma_S - \gamma_L\cos\theta \quad (8)$$

There are several other methods for obtaining surface tension values; however, the appropriateness of these methods for the probing of particular polymer/solvent combinations remains a subject of debate [44–46]. Fowkes [47] and Neumann's [44,48] approaches were chosen in this study to provide a basis for comparison.

Fowkes method is commonly used for the determination of the surface free energy of polymeric materials [49]. Two-phase systems are investigated that contain a substance (solid or liquid) in which only the dispersion interactions appear. Considering such systems, Fowkes determined the surface free energy corresponding to the solid-liquid interface using the following equation [49]:

$$\gamma_{SL} = \gamma_S + \gamma_L - 2(\gamma_S^{LW}\gamma_L^{LW})^{0.5} \quad (9)$$

According to Fowkes [50,51], the combination of Equations (8) and (9) yields the formula that enables one to calculate the surface free energy of a solid for which $\gamma_S = \gamma_S^{LW}$ is valid [49]:

$$\gamma_S = \gamma_S^{LW} = \gamma_L^2(1 + \cos\theta)^2/4\gamma_L^{LW} \quad (10)$$

If the measuring liquid is a dispersive one ($\gamma_L = \gamma_L^{LW}$), Equation (10) simplifies to:

$$\gamma_S = \gamma_S^{LW} = 0.25\gamma_L(1 + \cos\theta)^2 \quad (11)$$

To determine γ_S of any solid, the CA for the solid is measured using the dispersion liquid. Then, γ_S^{LW} is calculated from Equation (11). Next, the CA (θ_p) is measured using a liquid for which $\gamma_L = \gamma_L^{LW} + \gamma_L^{AB}$. The γ_S^{AB} can be estimated using [49]:

$$\gamma_S^{AB} = [0.5\gamma_L(1 + \cos\theta_p) - (\gamma_S^{LW}\gamma_L^{LW})^{0.5}]^2/\gamma_L^{AB} \quad (12)$$

Fowkes method is based on the independence and additivity of the dispersion and polar interactions [49]. On the other hand, Neumann's approach derives the SFT from a purely thermodynamic point of view and, therefore, neglects the molecular origins of SFT [7]. However, this is the only theory that allows the calculations to be done by using just one probing liquid. The following equation provides a method for calculating the surface energy of a solid from a single CA value [44,48]:

$$\cos\theta = -1 + 2\sqrt{\frac{\gamma_S}{\gamma_L}}e^{-\beta(\gamma_L - \gamma_S)^2} \quad (13)$$

where β is an experimentally-derived constant (β ≈ 0.0001247) [49].

2.5. Determination of Roughness and Wetting Behaviour of Surfaces

To analyse the effect of surface roughness on the wetting properties of the pp–GT thin films, the polymer was deposited on glass, silicon (Si), silicon dioxide (SiO_2) and indium tin oxide (ITO) substrates using RF plasma polymerization at 75 W RF power. The surface morphology and roughness parameters of the films were determined from AFM images acquired on a NT-MDT NTEGRA Prima AFM operating in semi-contact (tapping) mode, using (NSC05, NT-MDT) cantilevers with a spring constant of 11 N/m, a tip radius of curvature of 10 nm, an aspect ratio of 10:1 and a resonance frequency of 150 KHz. 3D interactive visualization and statistical approximation was used to analyse the topographic profiles of the surfaces. Scanning was performed perpendicular to the axis of the cantilever at a rate of typically 1 Hz, with scan areas of 1 μm × 1 μm, 10 μm × 10 μm and 50 μm × 50 μm.

3. Results and Discussion

3.1. Chemical Analysis of pp–GT Films

The monomer, 1-isopropyl-4-methyl-1,4-cyclohexadiene ($C_{10}H_{16}$), belongs to the group of monocyclic Terpinenes commonly designated as monoterpenes. It contains two double bonds in its ring-structure, which are not conjugated (1,4-diene group).

Due to the highly unsaturated nature of cyclohexa-1,4-diene with its 4 sp^2 carbon atoms, γ-Terpinene is considered almost planar. The molecular structure is characterized by one conformationally relevant internal rotation axis (C^1–C^7), which allows for the formation of various conformations (Figure 1). Density functional theory (DFT) calculations conducted by Marzec and co-workers led to the identification of three minima on the molecule's potential energy surface [35]. According to the orientation of the C^2–C^1–C^7–H^7 dihedral angle (α), the conformers were named trans, gauche+ and gauche−. The gauche+ (α = 47.5°) and gauche− (α = −47.5°) conformers (C_1) are mirror images, while the trans-like (α = 180.0°) conformer has C_s symmetry. Since different conformations characterize the amount and type of contact between adjacent atoms or groups, these data are important for defining the macroscopic properties of the material.

The IR spectra of the monomer, 1-isopropyl-4-methyl-1,4-cyclohexadiene, and the various pp–GT thin films are shown in Figure 2. Characteristic IR vibrations are summarized in Table 1. For the monomer, multiple C–H stretching vibrations were found as a strong signal between 2818 and 2960 cm^{-1}, whereas the corresponding C–H bending vibrations appeared as broad signals and with weak to medium intensities in the range of 1300 to 1466 cm^{-1}, confirming the population of various conformers [35]. The stretching vibrations of the C–C bonds were observed in the fingerprint region below 1200 cm^{-1}. In contrast, no clear stretching vibrations of the C=C bonds could be observed. The data collected was in agreement with some previous publications reporting the interpretation of vibrational spectra of 1-isopropyl-4-methyl-1,4-cyclohexadiene [52,53]. Comparing the IR spectra for the pp–GT thin films with that of the monomer, it is evident that the number of absorption frequencies in the spectra has reduced significantly upon polymerization, particularly in the fingerprint region of the spectrum (1500 cm^{-1} and below). Peaks also broadened for the pp–GT thin films, indicating very high degrees of polymerization. This is further supported by the disappearance of the =C–H vibration at 3088 cm^{-1}.

Electron-generated dissociation of GT monomer (rather than thermally excited or by direct chemical reaction) forces the input RF power to strongly affect the nature of the chemically-reactive species that engage in polymerization and film formation. Considering the bond strengths for 1-isopropyl-4-methyl-1,4-cyclohexadiene, the C–C single bonds are likely to dissociate first to form reactive fragments. Dissociation of higher energy bonds will occur when RF power is increased, and hence, the resultant fragmentation of the precursor molecule and subsequent crosslinking will increase. The double bonds in 1-isopropyl-4-methyl-1,4-cyclohexadiene are likely to undergo saturation through a reaction with these reactive fragments. Furthermore, the temperature of the substrate will also increase as a result of the exposure of the substrate to a large amount of energy. This will result in a reduction in the retention of the original precursor moieties [54].

Figure 2. FTIR spectra (% transmittance *vs.* wavenumber, cm^{-1}) for γ-Terpinene monomer and pp–GT thin films.

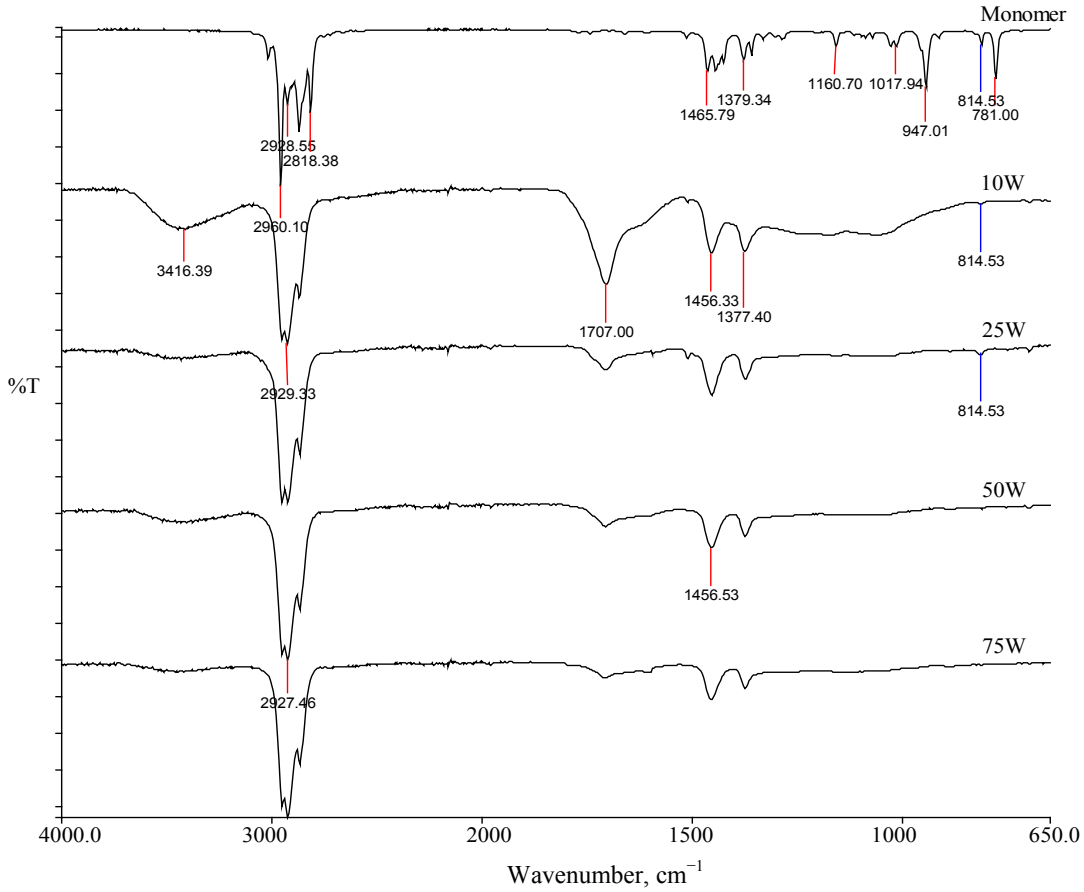

Table 1. FTIR assignments for γ-Terpinene monomer and plasma-polymerized γ-Terpinene (pp–GT) films, adapted from [55].

Assignment	Group Frequency, cm^{-1}	
	Monomer	**pp–GT Films**
ν (OH) of water	absent	3416 (medium to weak)
ν (=C–H)	3088 (weak)	absent
ν (C–H)	2818–2960 (medium to strong)	2872–2960 (strong)
ν (C=O)	absent	1707 (medium to weak, broad)
δ (C–H)	1300–1466 (medium to weak)	1377, 1456 (medium, broad)
ν (C–C)	947–1161 (strong to weak)	unresolved or absent
ω (C–H)	781 (strong), 815 (medium)	815 (medium to absent)

Vibrational modes: ν = stretching, δ = bending, ω = out of plane bending.

A broad absorbance band emerged at 3416 cm^{-1} (Figure 2) in the pp–GT spectrum that is considered to be the O–H stretching vibration of residual water. This is further supported by the absence of a C–O vibration. The infrared band associated with C–H stretching vibrations observed for the monomer also remained for the polymeric films; their intensity broadened, thus suggesting high degrees of cross-linking. Absorptions corresponding to C–H bending vibrations (between 1300 and 1466 cm^{-1}) decreased in magnitude and broadened with higher input RF power. Likewise, skeletal C–C vibrations between 947 and 1161 cm^{-1} vanished completely. A peak emerged at 1707 cm^{-1}, indicating the presence

of carbonyl groups (C=O stretch), which were presumably formed from the reactions of radical intermediates with residual molecular oxygen and subsequent decompositions. The peak, however, decreased and eventually almost disappeared with higher RF power, possibly due to increased fragmentations and combinations of the carbon skeleton under these extreme conditions. The presence of C=O bonds in the polymer films obtained at lower powers aligns with the differences in the properties of these materials. In general, polymer materials containing C=O (and –OH) groups are characterized by a high-dielectric constant, because of their high polarizability [56] and lower hydrophobicity. In addition, these polymers are likely to be more unstable (chemically and mechanically) compared to hydrocarbon polymers, as C=O (and –OH) bonds allow increased interactions with polar solvents. The CA investigations in this study revealed that pp–GT films deposited at lower RF power were indeed less stable when in contact with common processing solvents, such as acetone or alcohol. The reduction or complete disappearance of the C=O moiety renders pp–GT more stable.

The FTIR findings are consistent with the results of elemental analysis (X-ray photoelectron spectroscopy (XPS)) of pp–GT thin films deposited at various RF power levels. The oxygen content significantly decreased from 11.8% to 2.1%, while the carbon fraction increased from 88.2% to 97.8% with RF deposition power increasing from 10 to 50 W (Table 2). This result showed a substantial reduction in magnitude of the H-bonded O–H stretch-related band for pp–GT fabricated under higher RF power conditions.

Table 2. Elemental composition of pp–GT thin films deposited at various RF power.

Peaks	Atomic Fraction, %		
	10 W	**25 W**	**50 W**
O 1s	11.8	5.3	2.1
C 1s	88.2	94.7	97.8

3.2. Contact Angle and Wettability

A CAH approach provides several parameters listed in Table 3, useful in quantitative evaluations of water/solid surface interactions. An increase in deposition power resulted in a greater values for the advancing CA and W_A and smaller values for the receding CA, CAH, γ_{SV} and W_S. The relatively low receding CA reflects higher liquid sorption and/or solid swelling observed in the films fabricated at lower RF power [39]. The relatively low CAH for films fabricated at high RF power may be the result of the lower content of unsaturated double bonds in the pp–GT films and the film being more chemically homogenous [57]. At high RF power, intense fragmentation takes place and a very little amount of the original monomer/oligomeric units get integrated into the film structure. At this condition, the plasma-polymerized film is also highly cross-linked, which prevents the rotational motion of the surface moieties away from the surface towards the bulk of the film. The low CAH for 75-W film is also consistent with the low surface roughness, which, in earlier investigations, was found to decrease with deposition power [26]. CAH increases, as the RF power is decreased, which might be attributed to the higher content of unsaturated double bonds in the pp–GT films and loose cross-linking [57]. Incorporation of many monomer and oligomer units also takes place during this process at low RF

power. These may lead to a decrease in the homogenous surface chemical composition and an increase in surface roughness with the decrease in RF power.

Table 3. Wettability parameters of pp–GT thin films deposited at various RF power derived from contact angle hysteresis (CAH).

RF Power, W	θ_A, °	θ_R, °	*CAH*, °	γ_{SV} (mJ·m^{-2})	W_A (mJ·m^{-2})	W_S (mJ·m^{-2})
10	63.14	8.28	54.86	44.60	105.69	−39.91
25	69.25	17.43	51.82	40.27	98.59	−47.01
50	72.98	29.15	43.83	38.39	94.11	−51.49
75	73.53	36	37.53	38.91	93.44	−52.16

Dynamic CAs determined using other probing liquids, e.g., DIM and EG, showed similar trends.

The surface hydrophobicity/hydrophilicity of the pp–GT films of different RF power levels for different solvents based on the static CA measurements are summarized in Table 4. Independent of thickness, the application of the pp–GT coating affected the static CA values for all three probing liquid ($p < 0.05$): water, EG and DIM. According to Olivares-Navarrete *et al*. [58] a similar phenomenon is observed for Niobium coatings. Significant differences in static CAs were observed in the case of water for pp–GT films fabricated at different RF power. In all other cases, CA values were found in the same range.

Table 4. Static CAs for pp–GT thin film surfaces. DIM, diiodomethane.

Sample, W	CA ± SD, °		
	Water	Ethylene Glycol	DIM
10	61.03 ± 1.79	36.29 ± 2.56	36.56 ± 1.29
25	68.93 ± 0.88	37.44 ± 2.03	36.47 ± 2.24
50	72.72 ±1.47	41.97 ± 3.60	36.58 ± 2.01
75	80.72 ± 1.94	49.33 ± 1.25	38.70 ± 3.45

The static CA data presents important information regarding interactions between the surface and the liquid system. A relatively high rate of change in the water CA signifies the reorientation of functionalities at the solid-solvent interface [59]. From the raw data for EG (Figure 3), an initial rapid drop in CA was attributed to the absorption of the solvent into the pp–GT thin film. Subsequently, the CA remained relatively stable for the duration of recording. While this rate of change was considered insignificant, the positive ramp suggested the occurrence of the reorientation of functionalities at the interface. For the DIM data, all of the films were stable with time, and the highest CA was found for films fabricated at 75 W. These results indicate that pp–GT is more stable as the RF power is increased, due to an increase in the degree of cross-link density associated with these deposition conditions [7].

The initial water CAs, θ_0 suggested that pp–GT thin films deposited at higher RF power were more hydrophobic compared to the films fabricated at lower RF power, with CAs of 61.0° (10 W) and 80.7° (75 W). This was attributed to the reduction of hydrophilic moieties at the top surface of the polymer and the decrease in the oxygen content associated with the higher deposition power.

Figure 3. Representative static CA curves for pp–GT thin films for (**a**) water; (**b**) EG and (**c**) DIM.

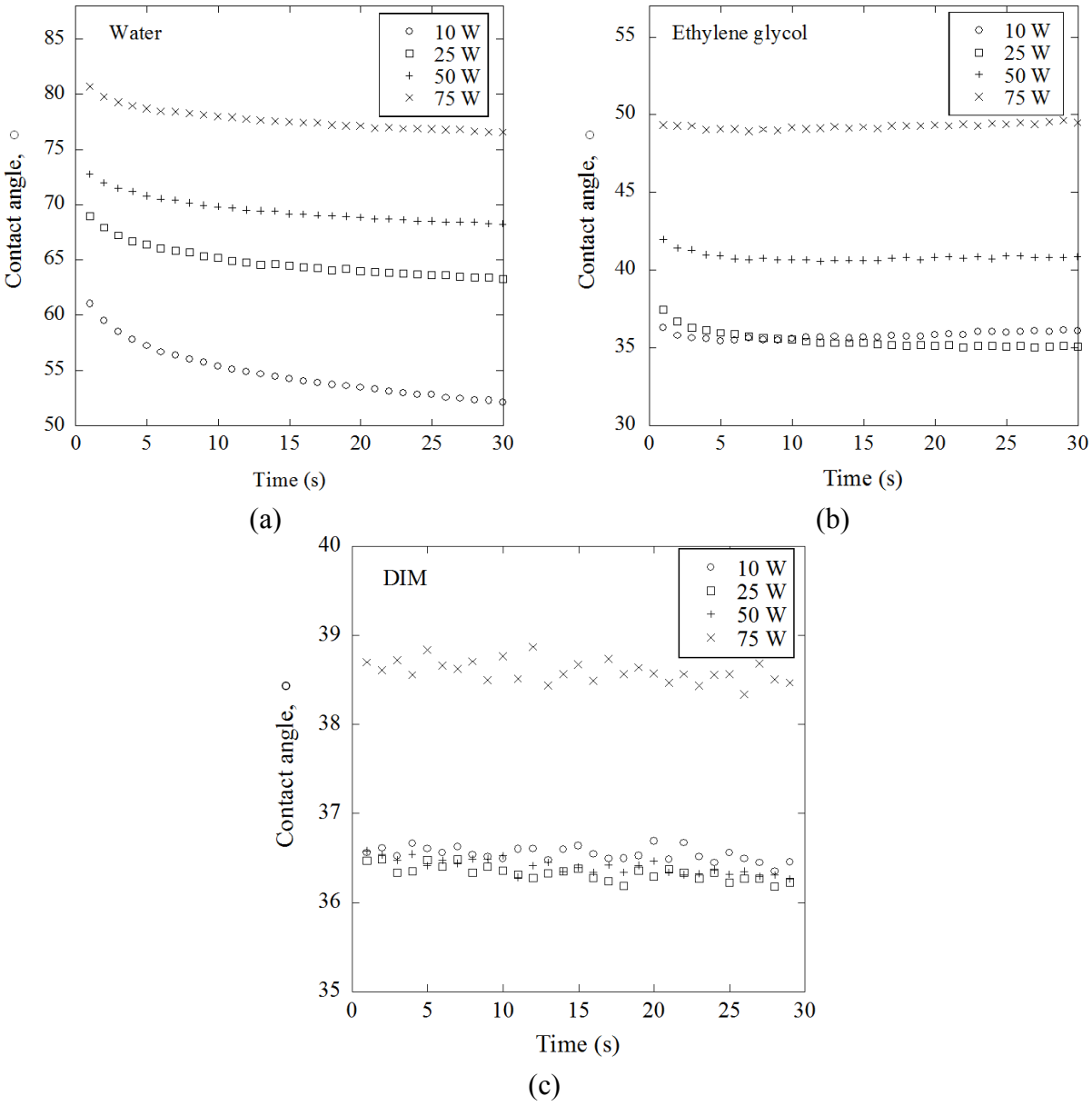

Investigating the evolution of the droplet profile may also be appropriate and meaningful to determine the wetting behaviour of thin films, especially if supported by considerations accounting for the phenomena involved at the solid/liquid interface [12]. The relationship between CA and the relevant surface phenomena can be simplified by the following general expression:

$$\theta(t) = \sum_{i=1}^{n} f_i(t) \tag{14}$$

where each $f_i(t)$ is related to one of the n independent phenomena involved (e.g., absorption, spreading, swelling and evaporation of the water drop). The derivative of $\theta(t)$ can be used to compute the θ evolution rate and predict the time required to reach the steady-state condition, $(\Delta\theta/\Delta t) \approx 0$.

$$\frac{\Delta\theta}{\Delta t} = \sum_{i=1}^{n} \frac{\Delta f_i(t)}{\Delta t} \tag{15}$$

The phenomena involved at the water droplet-polymer interface can also be profitably investigated by using a suitable image analysis procedure [12]. A reliable description of droplet evolution that depends on two major effects, namely, absorption and spreading, can be determined from a combined trigonometric (detection of θ) and geometric (changes in the droplet shape) approach. The absorption effect can be described as the sinking of the water droplet beneath the contact surface, with decreases in its volume (V) and contact area, but the volume is not affected in case of spreading effect, although it widens the contact area [12]. In this work, the detection of θ and the shape parameters (droplet height h, basal radius r, contact area and droplet volume V) determined by image analysis were used to describe absorption and spreading quantitatively, as well as their correlation with the surface topography of the films.

The evaporation of a sessile droplet can go through four consecutive stages: (i) spreading until the value of static advancing CA is reached; (ii) evaporation proceeds with a constant contact area and decreasing CA, until it reaches the receding value; (iii) evaporation with a constant receding CA and decreasing radius of the contact line; and (iv) evaporation with a decrease of both the radius of the contact line and CA until the droplet disappears. During Stage (i), the evaporation can be neglected [60]. In the present work, the contribution of evaporation to the total water droplet kinetics was examined directly by measuring the CA on pp–GT thin films. For films fabricated at 50 and 75 W, spreading phenomena was found to be in effect until static CA of 69.9° and 78.0° was reached. No significant difference between the water droplet volume values (Table 4) was found throughout the analysis. The effect of evaporation is therefore considered to be negligible for pp–GT thin films fabricated at 50- and 75-W RF power. The same trend was observed in case of poly(ethylene terephthalate) (PET) [12].

Given the negligible evaporation effects, the CA evolution was considered to be related to changes in the droplet volume and the solid/liquid surface contact area for all pp–GT thin films tested in this work. This would indicate that, at least at the early stages, two different physicochemical phenomena are occurring at the solid/liquid interface: absorption and spreading. At first glance, rather large differences in θ were observed within the first 30 s for the 10- and 25-W polymer thin films, which were confirmed by the data reported in Table 5 and by Figure 4.

The water droplet profile began to change once the droplet was in contact with the 10-W polymer thin film. Figure 4 shows that over the period of 0–10 s, the perceptible increase in the solid/liquid contact area on the pp–GT film fabricated at 10 W was accompanied by a decrease in volume, possibly because of the spontaneous diffusion of water inside the thin film via absorption. The drop surface area data suggests that, after this early phase, spreading began to take place and contributed to the overall kinetics of the evolution of the droplet profile. Both the absorption and spreading phenomena then continued to contribute, until the end of the 30-s period of analysis. The 25-W pp–GT thin film showed the same phenomena over the 0–10-s period. There was an early interaction of the surface and water that is evident from the increased drop surface area (Figure 4). After this early phase, the solid/liquid contact area remained stable for the remainder of the period of analysis. However, a decrease in volume suggests the evaporation phenomenon for that period of analysis.

Table 5. Main parameters derived from static water CA measurement of pp–GT thin films.

RF Power, W	$\Delta\theta_{t30\text{-}t0}$, ° [a]	$\Delta V_{t30\text{-}t0}$, µL [b]	$\Delta A_{t30\text{-}t0}$, mm^2 [c]	Phenomenon
10	−8.91 ± 0.72	−0.08 ± 0.07	0.51 ± 0.79	Absorption + spreading
25	−5.67 ± 1.09	−0.08 ± 0.05	0.15 ± 0.27	Absorption + evaporation
50	−4.47 ± 0.44	−0.07 ± 0.05	0.05 ± 0.11	Evaporation
75	−4.16 ± 0.03	−0.06 ± 0.01	−0.04 ± 0.02	Evaporation

[a] The CA variation during the time of analysis (30 s); [b] water droplet volume variation; [c] drop surface area variation.

Figure 4. Solid/liquid contact area (mm^2) evolution over time (30 s) for pp–GT thin films.

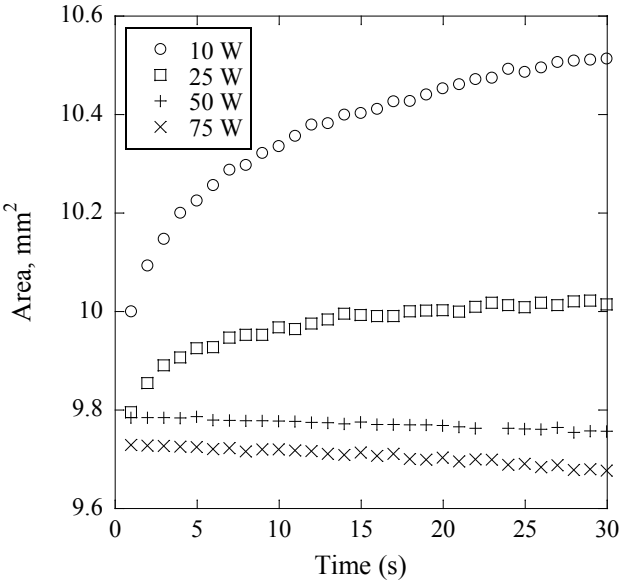

Figure 5 illustrates that curves for the pp–GT thin films fabricated at 10 W and 25 W could not attain a zero-order-rate state at the end of the 30-s analysis. Both absorption and spreading were therefore still occurring at the end of the analysis period at the solid/liquid interface.

Figure 5. The first derivative of the curves of static water CA evolution during the 30-s period of analysis.

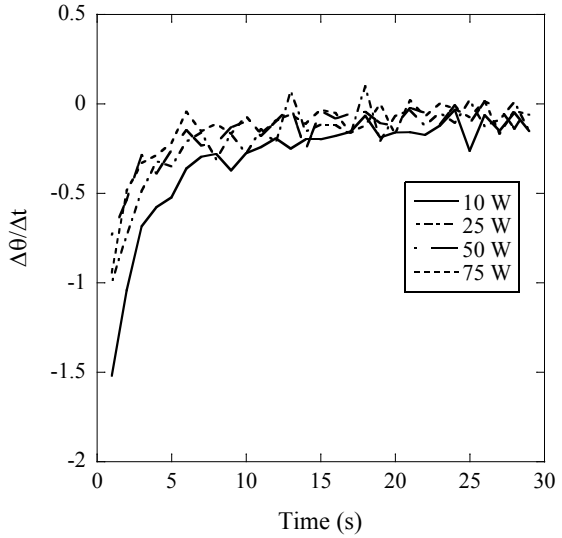

The water droplet profile of 50- and 75-W polymer thin films did not change substantially during the 30-s analysis, although the difference between θ_0 and θ_{30} was statistically significant ($p < 0.05$) (Table 4). According to the literature, these observations may be due to two factors: (i) the inclination of the water droplet to minimize its surface area when interacting with the polymer surface, which is capable of changing its free energy through the reorientation of certain polymer chains exposed at the solid/air interface [61]; and (ii) molecular conformation changes. The preferred orientation of functional groups could justify the θ values, as well as the decrease in the drop surface area (Figures 4 and 6).

Figure 6. Experimental heights of the droplet on pp–GT thin films.

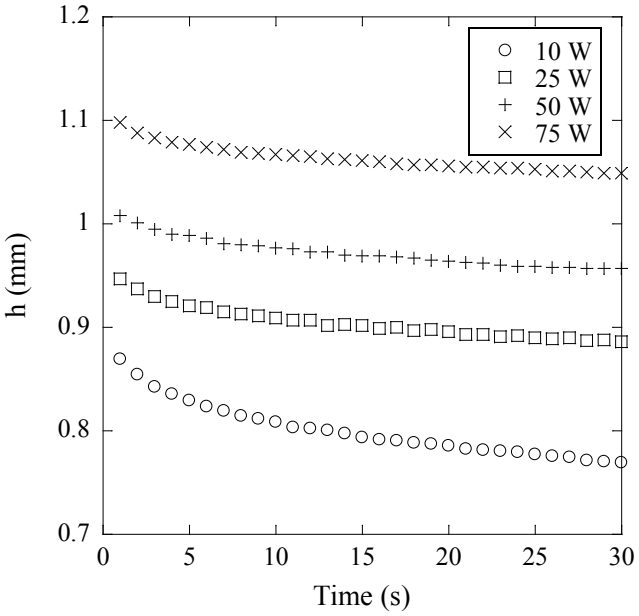

3.3. Contact Angle/Image Analysis Combined Approach

To gain information on the main driving forces governing drop evolution on pp–GT thin film surfaces, such as absorption, spreading, swelling and evaporation, and to determine their individual contributions to the overall wetting phenomenon, a combined CA/image analysis approach was adopted that enabled the spherical condition of the dome formed by the droplet at the solid/liquid interface to be assessed.

The shape of the water droplets changed with time, and pp–GT thin film fabricated at 10 W showed the most profound change observed from the CCD camera images. Physicochemical features of 10 W films and the inherent structural flexibility can explain this phenomenon. These two factors are recognized as crucial factors in aggregation on the molecular level [62]. The 10-W pp–GT thin films also showed the largest variations for both spreading and absorption. However, smaller effects were observed for 75-W films, where the evaporation phenomenon was detected, but was almost negligible ($\Delta A = -0.01$ mm^2). An indication of this is also provided in Figure 6, where the experimental heights of the water droplet are displayed.

As noticeable from Figure 6, the height of the water droplet on pp–GT thin film fabricated at 10 W dropped further and at a faster rate compared to the respective heights of droplets on films fabricated at

other RF powers. This may be due to the wider and deeper undulations present in the 10 W film (Figure 7) compared to the films fabricated at 25, 50 and 75 W.

Figure 7. AFM image (1 × 1 μm^2) of the pp–GT film fabricated at 10 W.

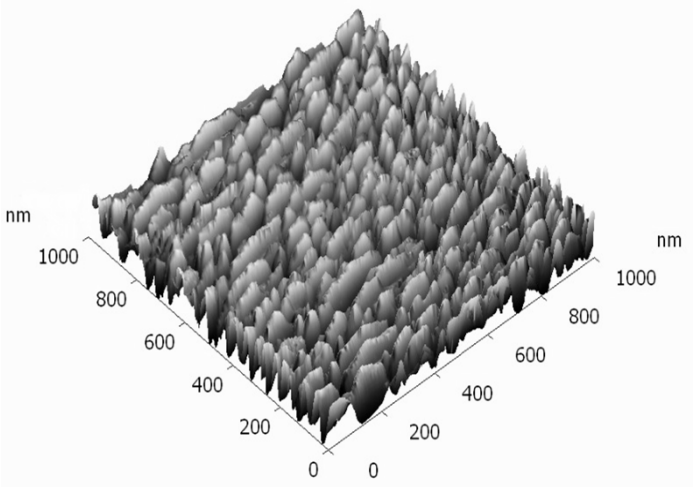

3.4. Effect of Surface Roughness on Wettability

Wetting of a surface by a liquid is influenced by the roughness of that surface [15]. Thin films of pp–GT were deposited at 75-W RF power on topographically-distinct surfaces of glass, Si, SiO_2 and ITO substrates to attain chemically similar, but morphologically different, pp–GT surfaces and, thus, to investigate the influence of roughness on the wetting properties of the material. Surface roughness was characterized by AFM, with the corresponding roughness values shown in Table 6. After the surface roughness characterization, wetting studies by CA measurements were carried out using the sessile drop technique, as described in the Experimental Section. A CA correlation with surface roughness, as determined by AFM, is evident from these results.

Table 6. RMS roughness and CA values of pp–GT thin films deposited on different substrates.

Substrate	RMS Roughness ± SD, nm	CA ± SD, °
Glass	0.30 ± 1.51	80.72 ± 1.94
SiO_2	5.06 ± 1.03	81.95 ± 0.98
Si	7.14 ± 1.58	82.08 ± 1.54
ITO	13.94 ± 1.27	83.80 ± 1.47

The measurement of the water CAs on the pp–GT films deposited on glass and SiO_2 substrates show a virtually constant or a very small increase in the static CA values (Table 6), while films deposited on Si and ITO present an increase by 2°–4°. This tendency, even if very small, confirms that the water CAs increase with the surface roughness. As expected from this limited variation in roughness, the variation range in the water CAs reported for pp–GT thin films was very small. The results from this work also show that surface roughness influences the wetting of the pp–GT, even at extremely low R_q values. Busscher *et al.* [63] and Hitchcock *et al.* [64] reported similar effects of roughness on the wettability of several polymers. The effect of surface roughness on the wettability of pp–GT is therefore needed to be considered for potential applications.

3.5. Surface Tension (SFT) Parameters

SFT parameters for pp–GT thin films fabricated at different RF power levels were derived using the Van Oss-Chaudhury-Good (VCG), Fowkes and Neumann approach and are summarized in Table 7. The CA data obtained for the solvents, together with the widely-used SFT parameters for water, DIM and EG [65] were employed in this study.

Table 7. The surface tension (SFT) components obtained via VCG, Fowkes and Neumann's approach for pp–GT thin films.

Approach	SFT Components, mJ/m^2	Solvent	10 W	25 W	50 W	75 W
VCG	γ^{LW}	–	41.3	41.3	41.3	40.3
	γ^{AB}	–	3.4	3.7	2.7	1.6
	$\gamma+$	–	0.2	0.3	0.2	0.1
	$\gamma-$	–	19.1	10.9	8.7	4.5
	γ_s	–	44.7	45	44	41.8
Fowkes	γ_s		52.6	48.8	47.1	43.4
Neumann	γ_s	water	40.1	33.6	30.6	24.5
		DIM	39.1	38.6	36.5	32.7
		EG	41.3	41.3	41.3	40.3

Most monopolar materials are water soluble [65] and their values of γ^- are relatively large. For all pp–GT thin films, γ^- was significantly higher than γ^+, indicating a monopolar nature. It is possible to use these values of γ^- to determine an upper limit above which solubility will occur. Van Oss *et al.* [66] demonstrated that for a given Solute 1 (monopolar surface 1)-solvent 2 (bipolar) combination, the following equation can provide that limit:

$$\gamma_{12}^{TOT} = (\sqrt{\gamma_1^{LW}} - \sqrt{\gamma_2^{LW}})^2 + 2(\sqrt{\gamma_1^+\gamma_2^-} - \sqrt{\gamma_1^-\gamma_2^+}) \quad (16)$$

Employing $\gamma_2^{LW} \approx 40$ mJ/m^2, it was found that Equation (5) becomes negative. Interfacial tension therefore becomes negative for $\gamma_1^- > 28.31$ mJ/m^2. A negative interfacial tension between the material and water indicates the possibility of the penetration of water into the material, leading to repulsion between the molecules or particles and promoting solubilisation [66]. The pp–GT thin films have $\gamma^- < 28.31$ mJ/m^2 (Table 6). The films are therefore not water soluble. The 75-W film gave the lowest γ^- value, indicating that the hydrophobicity of the polymer increased with RF power.

The results obtained using Fowkes approach roughly compare with those obtained via VCG and Neumann's approaches. However, the VCG and Fowkes approaches are expected to be more accurate, as they require more than one CA measurements to determine SFT values. There was some variance in the values obtained using Neumann's approach between different solvents for each polymer film (Table 6). These values are smaller than those found with VCG approach, with the exception of the values for DIM. The total SFT (γ_s) was found between 41 and 45 mJ·m^{-2} for all samples investigated using the VCG approach. Values between 43 and 52 mJ·m^{-2} were found using the Fowkes approach. This is similar to the value of ≈44 mJ·m^{-2} for PET obtained by Wu *et al.* [67], as well as 42 mJ·m^{-2} for PMMA. The values are also consistent with those reported for plasma thin films deposited from other secondary plant metabolites, where total SFTs of 45–48, 36–40 and 31–37 mJ·m^{-2} were found for thin

films derived from linalyl acetate [68], *Lavandula angustifolia* essential oil [7] and terpinen-4-ol [69], respectively.

3.6. Wetting Behavior

The wettability of each solution on the pp–GT surface can be quantified by computing the spreading parameter $\Delta W = \gamma_L(\cos\theta - 1)$ [70]. It shows the extent to which the liquid will adhere to the surface relative to itself and, hence, indicates the ability of a liquid drop to stick to the solid surface during solution processing [71].

The pp–GT thin films fabricated at low RF power were characterized by increased wettability (Table 8). It is also observed that EG and DIM wets the pp–GT surface better than water. At $\theta = 0°$ and $\Delta W = 0$, the liquid can adhere well to the surface of the solid, and hence, complete wetting is observed. It is to be noted that the value of the work of spreading, W_S determined from the advancing and receding CAs are almost similar to the values of ΔW (calculated in this section), which gives the validation of the investigation.

Table 8. Spreading parameter (ΔW, mN/m) of pp–GT thin films.

Solvent	10 W	25 W	50 W	75 W
Water	−37.54	−46.63	−51.18	−61.10
EG	−9.31	−9.89	−12.31	−16.72
DIM	−9.99	−9.95	−10.00	−11.15

Another important illustration of the wetting behaviour of liquids on the pp–GT thin film surface can be performed from their wetting envelopes. These are the lines of constant equilibrium CA on a plot of the polar fraction (γ_L^{AB}) *versus* the dispersive fraction (γ_L^{LW}) of the liquid determined from the following equation [68]:

$$(1 + \cos\theta_a)\gamma_L = 2\left(\sqrt{\gamma_s^{LW}\gamma_L^{LW}} + \sqrt{\gamma_s^{AB}\gamma_L^{AB}}\right) \quad (17)$$

Figure 8 demonstrates the degree to which various liquids wet the pp–GT film surfaces fabricated at different RF power if γ_L^{AB} and γ_L^{LW} are known. It also illustrates the surface properties of ideal liquids for solution processing on the pp–GT thin films. By placing a boundary on the curve at a CA of 0°, complete wetting behavior can be determined. Liquids with surface energy components that lie above the line of $\theta = 40°$ will not wet the surfaces of pp–GT films sufficiently to enable suitable film formation from solution processing [71]. The points for water are lying on or between the 60° and 80° contour of the pp–GT wetting envelope, which means that it will not wet a pp–GT film surface, but rather, show a CA between 60° and 80°. This behaviour may be desirable if these films are considered as mechanically-flexible encapsulating coatings for organic electronics. The behaviour of chloroform and chlorobenzene was also examined, as these solvents are commonly used in the deposition of organic semiconducting layers from solution [72]. Both of them are found to lie within the 0° contour, indicating that each solvent will wet the pp–GT surface completely. If complete wetting of the surface by solution processing is needed for a specific application, both of these solvents would be appropriate in conjunction with the pp–GT thin film surface.

Figure 8. Wetting envelopes at 0°, 20°, 40°, 60° and 80° using surface tension components for pp–GT samples fabricated at (**a**) 10 W; (**b**) 25 W; (**c**) 50 W and (**d**) 75 W.

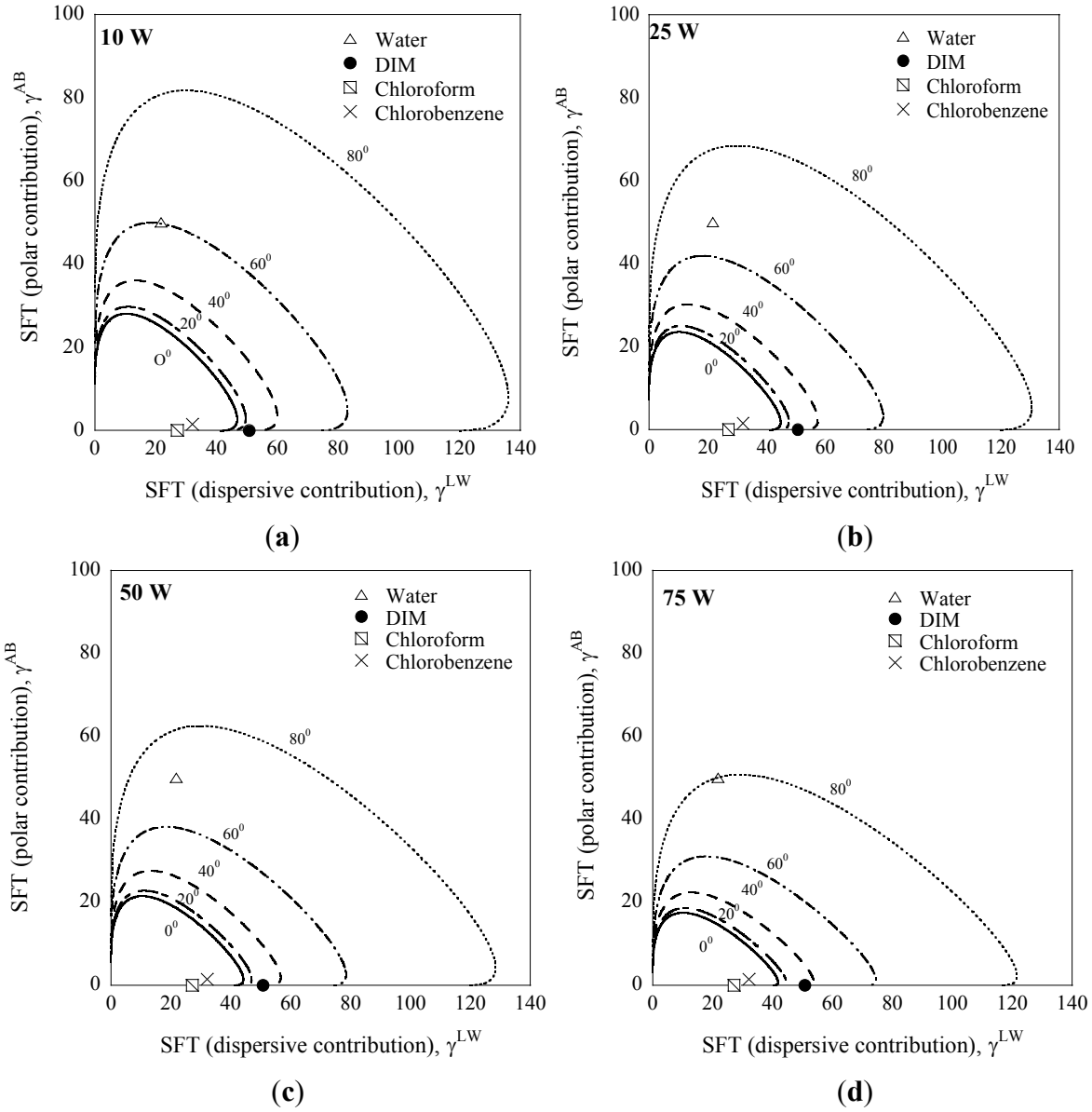

3.7. The Interfacial Tension and Solubility

The SFT parameters obtained using the VCG, Fowkes and Neumann's approach were used to calculate the interfacial tension between the solid and liquid given by Equations (7) and (8). The solubility of the solid (ΔG_{121}) in that liquid was then determined by incorporating interfacial tension values into Equation 6. Results using Equations (6)–(8) are presented in Table 9.

For $\Delta G_{121} >> 0$, the polymer is solvophilic for the solvent; for $\Delta G_{121} << 0$, the polymer is solvophobic for the solvent; for $\Delta G_{121} \approx 0$, the polymer is partially dissolved in the solvent. The values obtained (Table 9) indicate that the pp–GT polymer is solvophobic, and the strongest solvophobic response was found to be assigned to water, which is expected, as the CA values for water are found to be the most stable. The absence of negative γ_{SL} and γ_{12} values for the solvents investigated (Table 9), indicates that pp–GT is insoluble in the three liquids. ΔG_{121} values increased in magnitude with

increasing RF power for all of the probe liquids, except DIM. This shows a less soluble behaviour for water and EG. However, measurements using DIM indicate swelling or partial dissolution of pp–GT thin films.

Table 9. ΔG_{121} values obtained using Equations (5)–(7) from the derived surface tension data.

Solvent	RF Power (W)	γ_s Data	SFT Parameters, mJ/m^2		Solubility, mJ/m^2	
			γ_{SL} (Equation (8))	γ_{12} (Equation (7))	$\Delta G_{121} = -2\gamma_{SL}$	$\Delta G_{121} = -2\gamma_{12}$
Water	10 W	VCG	9.43	9.41	−18.86	−18.82
		Fowkes	17.34		−34.68	
		Neumann	4.84		−9.68	
	25 W	VCG	18.85	18.82	−37.7	−37.64
		Fowkes	22.6		−45.2	
		Neumann	7.47		−14.94	
	50 W	VCG	22.37	22.39	−44.74	−44.78
		Fowkes	25.47		−50.94	
		Neumann	9		−18	
	75 W	VCG	30.11	30.11	−60.22	−60.22
		Fowkes	31.67		−63.34	
		Neumann	12.80		−25.6	
EG	10 W	VCG	6.01	6.03	−12.02	−12.06
		Fowkes	13.92		−27.84	
		Neumann	0.45		−0.9	
	25 W	VCG	6.92	6.99	−13.84	−13.98
		Fowkes	10.67		−21.34	
		Neumann	0.51		−1.02	
	50 W	VCG	8.31	8.32	−16.62	−16.64
		Fowkes	11.41		−22.82	
		Neumann	0.79		−1.58	
	75 W	VCG	10.57	10.67	−21.14	−21.34
		Fowkes	12.13		24.26	
		Neumann	1.45		−2.90	
DIM	10 W	VCG	3.89	3.87	−7.78	−7.74
		Fowkes	11.8		−23.6	
		Neumann	0.5		−1	
	25 W	VCG	4.17	4.17	−8.34	−8.34
		Fowkes	7.92		−15.84	
		Neumann	0.49		−0.98	
	50 W	VCG	3.2	3.19	−6.40	−6.38
		Fowkes	6.30		−12.60	
		Neumann	0.5		−1	
	75 W	VCG	2.20	2.21	−4.40	−4.42
		Fowkes	3.76		7.52	
		Neumann	0.61		−1.22	

According to the wetting envelopes for pp–GT thin films, the CAs for several important organic solvents typically used in organic electronics, e.g., chloroform and chlorobenzene, will be too low to be determined experimentally. Therefore, the parameter θ_S is assumed to be 0° for the purpose of calculating

the solubility values for these solvents. These values were found to be strongly negative, indicating that the pp–GT films are insoluble for solvents employed in the processing of organic electronics.

4. Conclusions

The pp–GT films were successfully prepared and characterized. An FTIR analysis confirmed that exposure to an RF plasma field can effectively initiate the polymerization of the monomer. Some functional groups observed in the monomer were retained during the polymerization process, but the C=O stretching vibration (observed in pp–GT spectra) was not present in the monomer spectrum. An increase in RF power resulted in a reduction of the magnitude of the remaining groups, which was attributed to increased fragmentation and, consequently, polymerization of the monomer. RF power can therefore be an effective tool for the fabrication of polymer thin films with tuned properties.

The pp–GT films exhibited different wetting properties, as indicated by the investigation of CA analysis and wetting envelopes. The trends observed were directed by two main phenomena at the solid/liquid interface, namely absorption and spreading, which affect the overall wetting behaviour. This interpretation of the data was based on the assessment of the geometry of the water droplet placed on the film surfaces. The greatest absorption was detected for 10-W pp–GT films while using water as the solvent. Improved stability was observed for films fabricated at higher RF power with the increased hydrophobicity of the polymer surface, from 61.0° (10 W) to 80.7° (75 W). The polymer demonstrated a strong electron donor component and a negligible electron acceptor component and was therefore monopolar in nature. Wetting curves showed that the samples became more hydrophobic as the deposition energy was increased. Chloroform and chlorobenzene were both found to fall within the 0° boundary, indicating that they would completely wet the surface. Solubility results confirmed that the polymer would resist solubilisation from the solvents investigated.

The wettability and compatibility of pp–GT thin films with solvents utilized in the manufacturing of organic electronic devices has been investigated in this paper. From the wettability studies, it is concluded that pp–GT layers are suitable for encapsulation purpose and also for use in a variety of organic electronic devices requiring solution-processed layers.

Acknowledgments

Jakaria Ahmad greatly appreciates the financial support from the James Cook University Postgraduate Research Scholarship (JCUPRS). Kateryna Bazaka acknowledges funding from James Cook university (JCU) and Australian Research Council (ARC) (No. DE130101550).

Author Contributions

Jakaria Ahmad fabricated the thin films, performed tests, measured and assessed thin film characteristics and prepared the manuscript. Kateryna Bazaka contributed towards development of the characterization methods, data analysis and preparation of the manuscript. Michael Oelgemoeller assisted in the interpretation and analysis of the IR spectra and the preparation of this manuscript. Mohan V. Jacob coordinated and managed the project and the overall preparation of the manuscript.

Conflicts of Interest

The authors declare no conflict of interest.

References

1. Ahmafd, J.; Bazaka, K.; Anderson, L.J.; White, R.D.; Jacob, M.V. Materials and methods for encapsulation of OPV: A review. *Renew. Sustain. Energy Rev.* **2013**, *27*, 104–117.
2. Koti, R.S.; Sanjaykumar, S.R.; Hong, S.-J.; Song, C.E.; Kang, I.-N.; Lee, S.K.; Shin, W.S.; Moon, S.-J.; Lee, J.-C. 3,8-Dialkoxynaphthodithiophene based copolymers for efficient polymer solar cells. *Sol. Energy Mater. Sol. Cells* **2013**, *108*, 213–222.
3. Prakash, S.; Chakrabarty, T.; Singh, A.K.; Shahi, V.K. Polymer thin films embedded with metal nanoparticles for electrochemical biosensors applications. *Biosens. Bioelectron.* **2013**, *41*, 43–53.
4. Hierso, J.; Boy, P.; Vallé, K.; Vulliet, J.; Blein, F.; Laberty-Robert, C.; Sanchez, C. Nanostructured ceria based thin films (≤1 μm) as cathode/electrolyte interfaces. *J. Solid State Chem.* **2013**, *197*, 113–119.
5. Sownthari, K.; Suthanthiraraj, S.A. Synthesis and characterization of an electrolyte system based on a biodegradable polymer. *eXPRESS Polym. Lett.* **2013**, *7*, 495–504.
6. Hazrati, H.D.; Whittle, J.D.; Vasilev, K. A mechanistic study of the plasma polymerization of ethanol. *Plasma Process. Polym.* **2014**, *11*, 149–157.
7. Easton, C.D.; Jacob, M.V. Solubility and adhesion characteristics of plasma polymerized thin films derived from Lavandula angustifolia essential oil. *J. Appl. Polym. Sci.* **2010**, *115*, 404–415.
8. Bazaka, K.; Jacob, M.; Truong, V.K.; Crawford, R.J.; Ivanova, E.P. The effect of polyterpenol thin film surfaces on bacterial viability and adhesion. *Polymers* **2011**, *3*, 388–404.
9. Graham, M.; Cady, N. Nano and microscale topographies for the prevention of bacterial surface fouling. *Coatings* **2014**, *4*, 37–59.
10. Geoghegan, M.; Krausch, G. Wetting at polymer surfaces and interfaces. *Prog. Polym. Sci.* **2003**, *28*, 261–302.
11. Bollström, R.; Tuominen, M.; Määttänen, A.; Peltonen, J.; Toivakka, M. Top layer coatability on barrier coatings. *Prog. Organ. Coat.* **2012**, *73*, 26–32.
12. Farris, S.; Introzzi, L.; Biagioni, P.; Holz, T.; Schiraldi, A.; Piergiovanni, L. Wetting of biopolymer coatings: Contact angle kinetics and image analysis investigation. *Langmuir* **2011**, *27*, 7563–7574.
13. Kylián, O.; Polonskyi, O.; Kratochvíl, J.; Artemenko, A.; Choukourov, A.; Drábik, M.; Solař, P.; Slavínská, D.; Biederman, H. Control of wettability of plasma polymers by application of Ti Nano-Clusters. *Plasma Process. Polym.* **2012**, *9*, 180–187.
14. Xie, W.; Wang, J.; Berndt, C.C. Spreading Behavior and morphology of ethylene methacrylic acid (EMAA) deposits via the flame spray process. *Coatings* **2012**, *2*, 76–93.
15. Wenzel, R.N. Resistance of solid surfaces to wetting by water. *Ind. Eng. Chem.* **1936**, *28*, 988–994.
16. Cassie, A.B.D.; Baxter, S. Wettability of porous surfaces. *Trans. Faraday Soc.* **1944**, *40*, 546–551.
17. Gallezot, P. Conversion of biomass to selected chemical products. *Chem. Soc. Rev.* **2012**, *41*, 1538–1558.
18. Ostrikov, K.; Neyts, E.C.; Meyyappan, M. Plasma nanoscience: From nano-solids in plasmas to nano-plasmas in solids. *Adv. Phys.* **2013**, *62*, 113–224.

19. Michelmore, A.; Gross-Kosche, P.; Al-Bataineh, S.A.; Whittle, J.D.; Short, R.D. On the effect of monomer chemistry on growth mechanisms of nonfouling PEG-like plasma polymers. *Langmuir* **2013**, *29*, 2595–2601.
20. Irimia-Vladu, M. "Green" electronics: Biodegradable and biocompatible materials and devices for sustainable future. *Chem. Soc. Rev.* **2014**, *43*, 588–610.
21. Bazmi, A.A.; Zahedi, G. Sustainable energy systems: Role of optimization modeling techniques in power generation and supply—A review. *Renew. Sustain. Energy Rev.* **2011**, *15*, 3480–3500.
22. Pongprayoon, U.; Soontornsaratune, P.; Jarikasem, S.; Sematong, T.; Wasuwat, S.; Claeson, P. Topical antiinflammatory activity of the major lipophilic constituents of the rhizome of Zingiber cassumunar. Part I: The essential oil. *Phytomedicine* **1997**, *3*, 319–322.
23. Jacob, M.V.; Bazaka, K.; Weis, M.; Taguchi, D.; Manaka, T.; Iwamoto, M. Fabrication and characterization of polyterpenol as an insulating layer and incorporated organic field effect transistor. *Thin Solid Films* **2010**, *518*, 6123–6129.
24. Taguchi, D.; Manaka, T.; Iwamoto, M.; Bazaka, K.; Jacob, M.V. Analyzing hysteresis behavior of capacitance–voltage characteristics of IZO/C60/pentacene/Au diodes with a hole-transport electron-blocking polyterpenol layer by electric-field-induced optical second-harmonic generation measurement. *Chem. Phys. Lett.* **2013**, *572*, 150–153.
25. Anderson, L.J.; Jacob, M.V. Effect of RF power on the optical and morphological properties of RF plasma polymerised linalyl acetate thin films. *Appl. Surf. Sci.* **2010**, *256*, 3293–3298.
26. Ahmad, J.; Bazaka, K.; Jacob, M. Optical and surface characterization of radio frequency plasma polymerized 1-isopropyl-4-methyl-1,4-cyclohexadiene thin films. *Electronics* **2014**, *3*, 266–281.
27. Bazaka, K.; Jacob, M.V.; Taguchi, D.; Manaka, T.; Iwamoto, M. Investigation of interfacial charging and discharging in double-layer pentacene-based metal-insulator-metal device with polyterpenol blocking layer using electric field induced second harmonic generation. *Chem. Phys. Lett.* **2011**, *503*, 105–111.
28. Bazaka, K.; Jacob, M.V.; Truong, V.K.; Wang, F.; Pushpamali, W.A.; Wang, J.; Ellis, A.; Berndt, C.C.; Crawford, R.J.; Ivanova, E.P. Effect of plasma-enhanced chemical vapour deposition on the retention of antibacterial activity of terpinen-4-ol. *Biomacromolecules* **2010**, *11*, 2016–2021.
29. Al-Burtamani, S.K.S.; Fatope, M.O.; Marwah, R.G.; Onifade, A.K.; Al-Saidi, S.H. Chemical composition, antibacterial and antifungal activities of the essential oil of Haplophyllum tuberculatum from Oman. *J. Ethnopharmacol.* **2005**, *96*, 107–112.
30. Cheng, S.-S.; Liu, J.-Y.; Hsui, Y.-R.; Chang, S.-T. Chemical polymorphism and antifungal activity of essential oils from leaves of different provenances of indigenous cinnamon (Cinnamomum osmophloeum). *Bioresour. Technol.* **2006**, *97*, 306–312.
31. Breitmaier, E. Selected syntheses of terpenes. In *Terpenes*; Wiley-VCH Verlag GmbH & Co. KGaA: Weinheim, Germany, 2006; pp. 119–159.
32. Gengenbach, T.R.; Griesser, H.J. Deposition conditions influence the postdeposition oxidation of methyl methacrylate plasma polymer films. *J. Polym. Sci. A* **1998**, *36*, 985–1000.
33. J. A. Wllllam Co., Inc. Homepage. Available online: http://www.jawoollam.com (accessed on 3 July 2011).
34. Easton, C.D.; Jacob, M.V. Optical characterisation of radio frequency plasma polymerised Lavandula angustifolia essential oil thin films. *Thin Solid Films* **2009**, *517*, 4402–4407.

35. Marzec, K.M.; Reva, I.; Fausto, R.; Proniewicz, L.M. Comparative matrix isolation infrared spectroscopy study of 1,3- and 1,4-Diene monoterpenes (α-Phellandrene and γ-Terpinene). *J. Phys. Chem. A* **2011**, *115*, 4342–4353.
36. O'Toole, L.; Beck, A.J.; Ameen, A.P.; Jones, F.R.; Short, R.D. Radiofrequency-induced plasma polymerisation of propenoic acid and propanoic acid. *J. Chem. Soc. Faraday Trans.* **1995**, *91*, 3907–3912.
37. Watts, J.F. High resolution XPS of organic polymers: The Scienta ESCA 300 database. G. Beamson and D. Briggs. 280pp., £65. John Wiley & Sons, Chichester, ISBN 0471 935921, (1992). *Surf. Interface Anal.* **1993**, *20*, 267–267.
38. Strobel, M.; Lyons, C.S. An essay on contact angle measurements. *Plasma Process. Polym.* **2011**, *8*, 8–13.
39. Yuan, Y.; Lee, T.R. Contact angle and wetting properties. In *Surface Science Techniques*; Bracco, G., Holst, B., Eds.; Springer: Berlin, Germany, 2013; Volume 51, pp. 3–34.
40. Pogorzelski, S.J.; Rochowski, P.; Szurkowski, J. Pinus sylvestris L. needle surface wettability parameters as indicators of atmospheric environment pollution impacts: Novel contact angle hysteresis methodology. *Appl. Surf. Sci.* **2014**, *292*, 857–866.
41. Chibowski, E. Surface free energy of a solid from contact angle hysteresis. *Adv. Colloid Interface Sci.* **2003**, *103*, 149–172.
42. Good, R.J. Estimation of surface energies from contact angles. *Nature* **1966**, *212*, 276–277.
43. Van Oss, C.J. Long-range and short-range mechanisms of hydrophobic attraction and hydrophilic repulsion in specific and aspecific interactions. *J. Mol. Recognit.* **2003**, *16*, 177–190.
44. Kwok, D.Y.; Neumann, A.W. Contact angle measurement and contact angle interpretation. *Adv. Colloid Interface Sci.* **1999**, *81*, 167–249.
45. Shalel-Levanon, S.; Marmur, A. Validity and accuracy in evaluating surface tension of solids by additive approaches. *J. Colloid Interface Sci.* **2003**, *262*, 489–499.
46. Deshmukh, R.R.; Shetty, A.R. Comparison of surface energies using various approaches and their suitability. *J. Appl. Polym. Sci.* **2008**, *107*, 3707–3717.
47. Fowkes, F.M. Additivity of intermolecular forces at interfaces. I. Determination of the contribution to surface and interfacial tensions of dispersion forces in various liquids. *J. Phys. Chem.* **1963**, *67*, 2538–2541.
48. Tavana, H.; Neumann, A.W. Recent progress in the determination of solid surface tensions from contact angles. *Adv. Colloid Interface Sci.* **2007**, *132*, 1–32.
49. Zenkiewicz, M. Methods for the calculation of surface free energy of solids. *J. Achiev. Mater. Manuf. Eng.* **2007**, *24*, 137–145.
50. Fowkes, F.M. Donor-Acceptor interactions at interfaces. *J. Adhes.* **1972**, *4*, 155–159.
51. Fowkes, F.M. Attractive forces at interfaces. *Ind. Eng. Chem.* **1964**, *56*, 40–52.
52. Daferera, D.J.; Tarantilis, P.A.; Polissiou, M.G. Characterization of essential oils from lamiaceae species by fourier transform raman spectroscopy. *J. Agric. Food Chem.* **2002**, *50*, 5503–5507.
53. Schulz, H.; Özkan, G.; Baranska, M.; Krüger, H.; Özcan, M. Characterisation of essential oil plants from Turkey by IR and Raman spectroscopy. *Vib. Spectrosc.* **2005**, *39*, 249–256.
54. Lopez, G.P.; Ratner, B.D. Substrate temperature effects on film chemistry in plasma deposition of organics. I. Nonpolymerizable precursors. *Langmuir* **1991**, *7*, 766–773.

55. Coates, J. Interpretation of infrared spectra, a practical approach. In *Encyclopedia of Analytical Chemistry*; John Wiley & Sons, Ltd.: Hoboken, NJ, USA, 2006.
56. Bazaka, K.; Jacob, M.V. Post-deposition ageing reactions of plasma derived polyterpenol thin films. *Polym. Degrad. Stab.* **2010**, *95*, 1123–1128.
57. Shi, L. The investigation of polymer surface dynamics modified by plasma using dynamic contact angle method. *Eur. Polym. J.* **2000**, *36*, 987–992.
58. Olivares-Navarrete, R.; Olaya, J.J.; Ramírez, C.; Rodil, S.E. Biocompatibility of niobium coatings. *Coatings* **2011**, *1*, 72–87.
59. Alexander, M.R.; Duc, T.M. A study of the interaction of acrylic acid/1,7-octadiene plasma deposits with water and other solvents. *Polymer* **1999**, *40*, 5479–5488.
60. Semenov, S.; Starov, V.M.; Rubio, R.G.; Agogo, H.; Velarde, M.G. Evaporation of sessile water droplets: Universal behaviour in presence of contact angle hysteresis. *Colloids Surf. A Physicochem. Eng. Asp.* **2011**, *391*, 135–144.
61. Holly, F.J.; Refojo, M.F. Wettability of hydrogels. I. Poly (2-hydroxyethyl methacrylate). *J. Biomed. Mater. Res.* **1975**, *9*, 315–326.
62. Podestà, A.; Indrieri, M.; Brogioli, D.; Manning, G.; Milani, P.; Guerra, R.; Finzi, L.; Dunlap, D. Positively charged surfaces increase the flexibility of DNA. *Biophys. J.* **2005**, *89*, 2558–2563.
63. Busscher, H.J.; van Pelt, A.W.J.; de Boer, P.; de Jong, H.P.; Arends, J. The effect of surface roughening of polymers on measured contact angles of liquids. *Colloids Surf.* **1984**, *9*, 319–331.
64. Hitchcock, S.J.; Carroll, N.T.; Nicholas, M.G. Some effects of substrate roughness on wettability. *J. Mater. Sci.* **1981**, *16*, 714–732.
65. Wu, S.; Shanks, R.A. Solubility study of polyacrylamide in polar solvents. *J. Appl. Polym. Sci.* **2004**, *93*, 1493–1499.
66. Van Oss, C.J.; Chaudhury, M.K.; Good, R.J. Monopolar surfaces. *Adv. Colloid Interface Sci.* **1987**, *28*, 35–64.
67. Wu, W.; Giese, R.F., Jr.; van Oss, C.J. Evaluation of the lifshitz-van der waals/acid-base approach to determine surface tension components. *Langmuir* **1995**, *11*, 379–382.
68. Anderson, L.; Easton, C.; Jacob, M. Compatibility of plasma-deposited linalyl acetate thin films with organic electronic device fabrication techniques. *J. Mater. Sci.* **2013**, *48*, 4851–4859.
69. Bazaka, K.; Jacob, M.V. Solubility and surface interactions of RF plasma polymerized polyterpenol thin films. *Mater. Express* **2012**, *2*, 285–293.
70. De Gennes, P.G. Wetting: Statics and dynamics. *Rev. Mod. Phys.* **1985**, *57*, 827–863.
71. Wobkenberg, P.H.; Ball, J.; Kooistra, F.B.; Hummelen, J.C.; de Leeuw, D.M.; Bradley, D.D.C.; Anthopoulos, T.D. Low-voltage organic transistors based on solution processed semiconductors and self-assembled monolayer gate dielectrics. *Appl. Phys. Lett.* **2008**, *93*, doi:10.1063/1.2954015.
72. Cheng, X.; Caironi, M.; Noh, Y.-Y.; Newman, C.; Wang, J.; Lee, M.J.; Banger, K.; Pietro, R.D.; Facchetti, A.; Sirringhaus, H. Downscaling of *n*-channel organic field-effect transistors with inkjet-printed electrodes. *Org. Electron.* **2012**, *13*, 320–328.